Intelligent Service Robotics
https://doi.org/10.1007/s11370-023-00497-z

ORIGINAL RESEARCH PAPER

Development of the sub-10 cm, sub-100 g jumping–crawling robot

Sojung Yim[1] · Sang-Min Baek[1] · Pilwoo Lee[1] · Soo-Hwan Chae[1] · Jongeun Lee[1] · Seok-Haeng Huh[2] · Gwang-Pil Jung[3] · Kyu-Jin Cho[1]

Received: 17 July 2023 / Accepted: 16 November 2023

Abstract
The accessible environment and locomotion performance of a robot are governed by the scale of the robot. The operating time and speed can be increased as the scale of the robot increases. However, the size of the robot does limit the accessible environment: the robot cannot pass through a space smaller than its size. Therefore, to explore an environment containing gaps, holes, and crevices, a small-scale robot is required. In this paper, we propose a sub-10 cm, sub-100 g scale jumping–crawling robot. The proposed robot consists of crawling, jumping, and self-righting mechanisms. The combination of crawling and jumping allowed the robot to overcome obstacles of various sizes. To reduce the weight and size of the robot, we employed a smart composite microstructures (SCM) design method and utilized a shape memory alloy (SMA) actuator. All the mechanisms and electronic components were compactly integrated into a single robot. The robot can crawl with the maximum speed of 3.94 cm/s (0.4 BL/s), and jump 19 cm which is 2.2 times its body height.

Keywords jumping–crawling robot · Mechanism design · Mobile robot · Multi-modal locomotion

1 Introduction

Locomotive robots have been developed for tasks such as surveillance, reconnaissance, and search and rescue in environments that are difficult and dangerous for humans to access. To explore the unrevealed task environment, a locomotive robot should deal with various types and sizes of obstacles. Therefore, robots with specific locomotive modes that can overcome particular obstacles have been developed, such as crawling robots [1–6], jumping robots [7–10], and climbing robots [11–14]. In addition, to improve locomotion performance, a wide range of research has been conducted, from biology [15–17] to engineering [1–14]. Furthermore, multi-modal robots, which integrate various locomotive mechanisms into a single body have been developed, such as jumping–crawling robots [18–23], jumping–gliding robots [24–27], and climbing-flying robots [28, 29]. By selectively performing suitable locomotion, a robot can overcome various types of obstacles; therefore, the accessible environment of the robot is expanded.

The accessible environment and locomotion performance of the robot are governed by its scale [30]. In dynamically similar locomotion, locomotion velocity is proportional to the square root of the characteristic length. Moreover, the mass-specific cost of transport is negatively correlated with body mass [15]. Consequently, the operating time and speed can be increased as the scale of the robot increases. However, the size of the robot does limit the accessible environment: the robot cannot pass through a space smaller than its size. Therefore, to explore an environment containing gaps, holes, and crevices, a small-scale robot is required. In addition, the lightweightness and stowability of the small-scale robot improve its transportability when multiple robots are carried to the task environment in swarm robotic applications. Especially, handheld-sized robots have the potential to be utilized in places where people are. Not only for open spaces, but these robots can also traverse through confined spaces, such as small gaps under a shelf, narrow gaps between walls and furniture, and small holes like inside of the pipeline. Besides the locomotive functionality of the robot, portability makes

Sojung Yim and Sang-Min Baek have contributed equally to this work.

✉ Kyu-Jin Cho
kjcho@snu.ac.kr

1 Department of Mechanical Engineering, Seoul National University, Seoul 08826, Republic of Korea

2 LIG NEX1, Unmanned Ground Systems, Gyeonggi-do 13488, Republic of Korea

3 Department of Mechanical and Automotive Engineering, SeoulTech, Seoul 01811, Republic of Korea

Published online: 29 December 2023

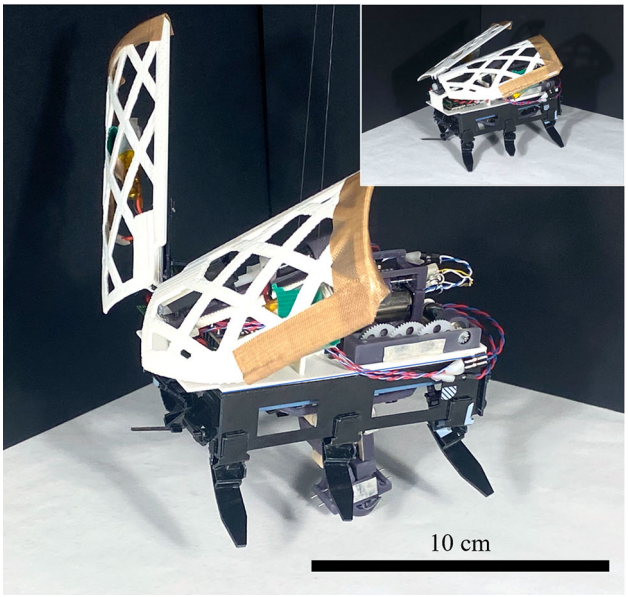

Fig. 1 Overall design of the proposed sub-10 cm, sub-100 g jumping–crawling robot

the robot to be easily carried and operated by individuals [31].

Smaller robot encounters relatively rough terrain as the relative size of the obstacles to the robot become larger [32]. In this regard, jumping–crawling is one promising terrestrial locomotion strategy for small-scale robots because the combination of crawling and jumping allows robots to overcome obstacles of various sizes. The robot crawls to traverse the ground consisting of slight bumps while maintaining its stability. Additionally, the robot can jump over large obstacles that it cannot crawl through. However, the development of a small-scale jumping–crawling robot is challenging in integrating various mechanisms into a single robot within a constrained size and weight. A jumping–crawling robot requires a crawling mechanism, jumping mechanism, and self-righting mechanism to upright its posture when the robot is turned over. Furthermore, a controller and batteries should be included to untether them for practical use. In the aspect of performance, the crawling legs and jumping legs become shorter as the robot's size is reduced. The shortened crawling leg decreases the stride length, which in turn reduces crawling speed. Additionally, the shortened jumping leg decreases the push-off distance and duration, which in turn reduces the output work for jumping. Also, for each mechanism, other mechanisms act as burdens, resulting in performance degradation of the multi-modal robot compared to the robot with a single mechanism.

In this paper, we propose a sub-10 cm, sub-100 g scale jumping–crawling robot, as shown in Fig. 1. The robot consists of a crawling mechanism (Fig. 2a), jumping mechanism (Fig. 2b), and self-righting mechanism (Fig. 2c). The robot can crawl through the gap with the size of the robot's frontal area, it can jump over obstacles higher than the robot's height, and the robot can recover to its upright posture using the self-righting mechanism. To reduce the weight and size of the mechanism, we employed the smart composite microstructures (SCM) design method [33] to the crawling mechanism and self-righting mechanism, and also utilized a shape memory alloy (SMA) to the triggering actuator of the jumping mechanism. Each mechanism is designed to avoid interference between parts within a limited size; hence, all the mechanisms and electronic parts are integrated into a single body. The size of the robot is (length) 9.8 cm × (width) 9 cm × (height) 8.8 cm and has a mass of 95.7 g including the controller and batteries. Table 1 shows that the proposed robot has the most compact form factor compared to previously developed robots. The list includes only untethered jumping–crawling robots with leg/wheg-based crawling mechanisms that are also capable of self-righting. Although the unavoidable scale effect reduces the locomotion performance of the proposed robot, its compactness enables the robot to pass through the smallest gap among the listed

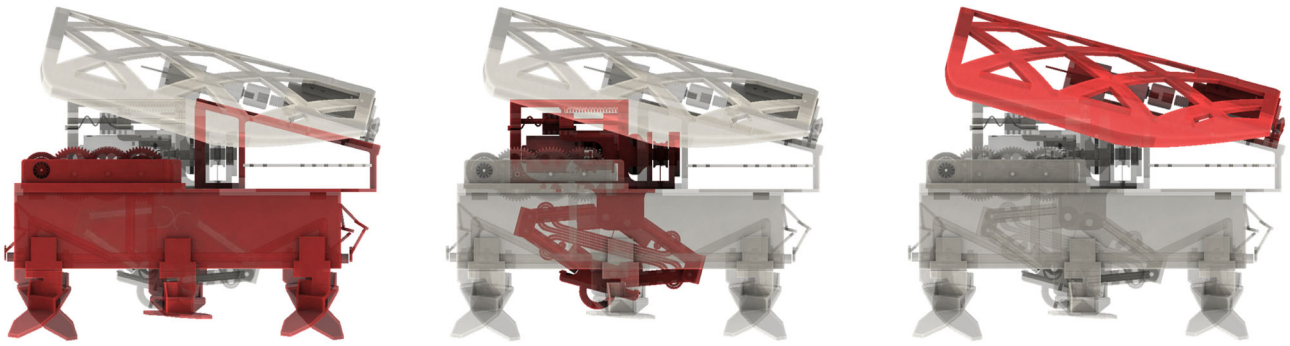

Fig. 2 Mechanism-wise composition of the robot. **a** highlights the crawling mechanism, **b** highlights the jumping mechanism, **c** highlights the self-righting mechanism

Table 1 Size and mass comparison of DC motor-driven jumping–crawling robots with leg/wheg-based crawling, jumping, self-righting, and untethered

Robot	Size				Mass
	Length (cm)	Width (cm)	Height (cm)	Volume (cm^3)	(g)
Mini-Whegs 9j [18]	10.4	N/A	N/A	N/A	191.4
JumpRoACH (including shell) [19]	19	11	8	1672	99
Agile jumping–crawling robot (including shell) [20]	16	11.5	8	2208	105
Proposed robot	9.8	9	8.8	776	95.7

robots. Additionally, the compact size enhances stowability and transportation efficiency when deploying multiple robots. This robot can crawl with the maximum speed of 3.94 cm/s (0.4 BL/s) and jump 19 cm which is 2.2 times its body height.

2 Design

The robot consists of the crawling, jumping, and self-righting mechanisms. These mechanisms are designed to be integrated into sub-10 cm, sub-100 g. The mechanism wise detailed approaches to meet this constraint are provided in the following sections.

2.1 Crawling mechanism

The hexapedal crawling mechanism requires two features-passive stability induced by tripod gait and discrete contact of the foot with the ground induced by the swing and stance gait cycle of the foot-to traverse through the bumpy field while maintaining its stability. In addition to the above-mentioned features, there are several requirements for fulfilling our design considerations. The crawling mechanism should be smaller than 10 cm, and it should be light to reduce the burden on jumping performance. In addition, the crawling mechanism requires two motors for steering.

We utilized the SCM design and fabrication method for the body of the crawling mechanism to make the complex crawling linkage structure compact and lightweight (Fig. 3a). Also, we designed a tripod coupler link pair to actuate the six legs using two geared motors while guaranteeing a mechanically constrained tripod gait (Fig. 3b, c). We employed a crawling linkage design from [1] and miniaturized it within a 10 cm size constraint; the mechanism is composed of parallel four-bar linkages and SCM universal jointed legs.

To embody the tripod gait, the tripod coupler link couples three legs, a front leg and a rear leg on the same side and a middle leg on the opposite side, making them work in phase. The leg set is connected to the crank of the geared motor by the tripod coupler link (Fig. 3c). As shown in Figs. 2b and 3c because the two tripod coupler links cross each other and

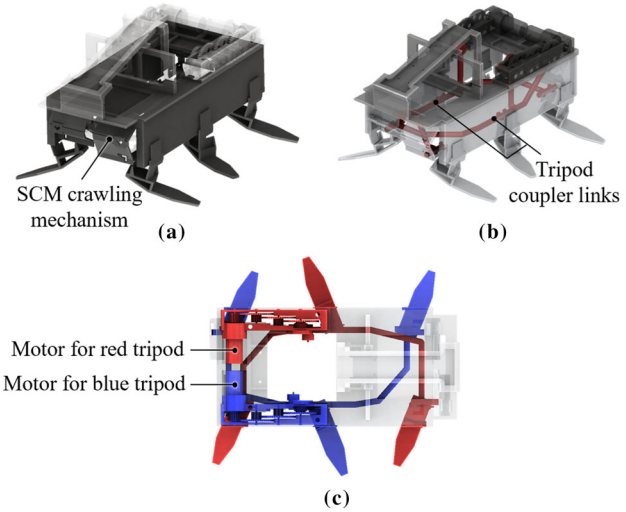

Fig. 3 Detailed composition of the crawling mechanism. **a** The crawling mechanism is based on the SCM design. The red-colored parts in **b** are the tripod coupler links. **b**, **c** show the connections between the legs and motors using tripod coupler links

the jumping mechanism is placed on the ventral side of the crawling mechanism, the tripod coupler links are designed to avoid interference between themselves and with the jumping mechanism.

2.2 Jumping mechanism

Our purpose is to design a jumping mechanism that is small enough to fit into the ventral cavity of the crawling mechanism. The jumping of a robot usually requires relatively higher power than the output of the equipped motor. Therefore, the mechanism requires the combined use of an energy storage component and an actuator, such as a spring and a motor, to amplify the output power. In addition, to jump at the desired timing, the mechanism requires a triggering method. Regarding these requirements, we developed a jumping mechanism composed of spring-embedded jumping linkage and an actuator package for energy loading and triggering (Fig. 4a).

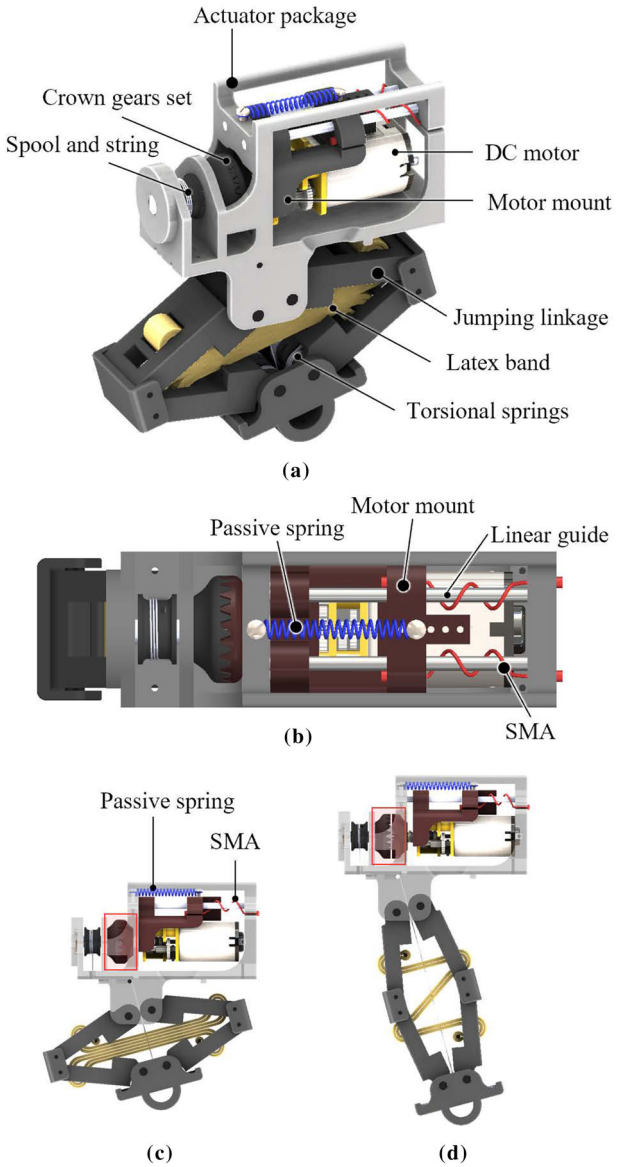

Fig. 4 Detailed composition of the jumping mechanism. **a** Overall components of the jumping mechanism **b** Top view of the jumping mechanism. The passive spring and SMA generate the movement of the motor mount along the linear guide. The passive spring pulls the motor mount leftward and the SMA pulls rightward. **c** Energy-loaded state of the jumping mechanism. In this state, the crown gears are engaged. **d** Energy-released state of the jumping mechanism. To trigger the jumping, the crown gears are disengaged

2.2.1 Jumping linkage

The jumping linkage is a rhombus-shaped four-bar linkage with rolling contact joints. We used one latex band and four steel torsional springs as elastic energy storage elements. The latex band is horizontally anchored to four links. When the linkage is vertically compressed, the distances between the spring anchoring points increase. Therefore, the latex band is stretched, and the elastic energy is stored. Torsional springs are located at the two joints at the bottom of the four-bar linkage. One end of the torsional spring is fixed to the bottom link of the linkage and the other end is fixed to the bottom plate. As the four-bar linkage is vertically compressed, the angle between the link and the bottom plate decreases, resulting in the energy storage of the torsional springs, as shown in Fig. 4c. To jump over the obstacle in a parabolic trajectory, the jumping linkage is fixed to the robot body with an inclination of 75 ° (Figs. 2b and 4d).

2.2.2 Actuation package design

To store energy in the spring, the motor gradually deforms it, and to release the energy, the triggering method promptly breaks the connection between the motor and spring. For these functions, we designed an actuator package composed of an energy-loading mechanism and triggering mechanism. We selected a geared DC motor as an energy loading actuator because it is suitable for continuous driving. Unlike the loading actuation, the triggering occurs intermittently; therefore, we utilized the SMA actuator, which is light and compact but inefficient in continuous actuation, as a triggering actuator. The energy-loading mechanism is composed of a geared DC motor, motor mount, clutching crown gear pair, and spool. One crown gear is fixed to the motor shaft and the other crown gear is fixed to the spool. The motor is fixed to the motor mount, and the motor mount can move along the linear guide. In this assembled configuration, the movement of the motor mount controls the engagement between crown gears (Fig. 4c and d). The triggering mechanism is in charge of controlling this movement. The triggering mechanism is composed of a passive spring and two SMA actuators. The passive spring maintains the engagement of the crown gears, whereas the contraction of the SMA actuator disengages the crown gears. When crown gears are engaged, the motor torque is transmitted to the spool, which winds a string tied to the bottom plate of the jumping linkage. The winding of the string compresses the jumping linkage vertically and stores energy in the springs. When the crown gears are disengaged, the jumping linkage and motor are disconnected, thereby triggering the jumping.

To select the geared DC motor, the motor torque required for energy loading was calculated. A lumped model was built as shown in Fig. 5, and the parameters related to the model are listed in Table 2. First, the spring potential energy V_k is calculated: it is the summation of the linear spring potential energy V_{linear} and torsional spring potential energy V_{torsion}. The length of the linear spring $s(\theta)$ with respect to the generalized coordinate θ is used to derive the V_{linear}. s_0 is the initial length of the spring.

$$s(\theta) = 2(d_2 + 2(l - s_2)\sin\theta) +$$

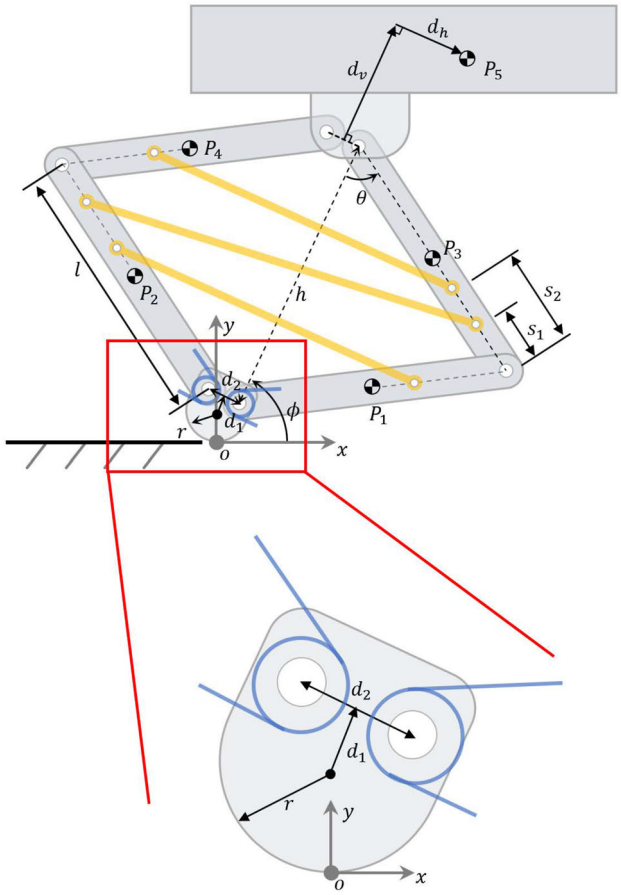

Fig. 5 Model of the jumping mechanism. Yellow indicates a linear spring, and blue indicates torsional springs

$$2(s_1{}^2 + (\frac{d_2}{2} + l\sin\theta)^2 - 2s_1(\frac{d_2}{2} + l\sin\theta)\sin\theta)^{\frac{1}{2}} \quad (1)$$

$$V_{\text{linear}} = \frac{1}{2}k_l(s(\theta) - s_0)^2 \quad (2)$$

$$V_{\text{torsion}} = 4 \times \frac{k_t\theta^2}{2} \quad (3)$$

$$V_k = V_{\text{linear}} + V_{\text{torsion}} \quad (4)$$

With the quasi-static assumption, the partial derivative of this potential energy with respect to the length of the string h can be treated as the required tension of the string for energy loading, F_{loading}. From the geometry of the linkage, Eq. (5) which relates the θ with the h is derived and applied to the differentiation process.

$$\theta(h) = \cos^{-1}(\frac{h}{2l}) \quad (5)$$

$$F_{\text{loading}} = \frac{-\partial V_k}{\partial h} \quad (6)$$

As a result, the required motor torque for energy loading $\tau_{loading}$ was calculated and represented with respect to the θ using Eq. (5). The result is illustrated in Fig. 6.

$$\tau_{\text{loading}} = r_{\text{pulley}}F_{\text{loading}} \quad (7)$$

As shown in Fig. 6, the maximum required torque is 29.1 mNm, therefore, we selected a geared DC motor with a higher torque output.

To select the passive spring and SMA actuators, we built two static models, as shown in Fig. 7. The parameters related to the model are listed in Table 2. The first model (Fig. 7c) was used to calculate the required force of the passive spring to firmly maintain crown gear engagement during energy loading. We analyzed this static model when the two gears were fully engaged. While loading energy, the reaction force between the crown gears tries to push the motor mount backward, and this backward movement can disengage the crown gears. To avoid this movement, the passive spring should apply the antagonistic force to the motor mount. Therefore, we calculated the minimum spring force which makes the x-direction component of the net force applied to the motor-connected crown gear less than zero (Fig. 7c). The equations describing this procedure are as follows:

$$\Sigma F_x = F_l\sin\theta_{\text{crown}} - F_{\text{p.s.}}\cos\theta_{\text{crown}} - f_l \le 0 \quad (8)$$

$$\Sigma F_y = N_l - F_l\cos\theta_{\text{crown}} - F_{\text{p.s.}}\sin\theta_{\text{crown}} = 0 \quad (9)$$

$$F_l = \frac{\tau_m}{r_{\text{crown}}} \quad (10)$$

$$f_l = \mu N_l \quad (11)$$

$F_{\text{p.s.}}$ is the passive spring force, F_l is the spring restoring force acting on the crown gear, N_l is the normal reaction force, f_l is the friction force between the two crown gears, and τ_m is the maximum required motor torque from Fig. (6). The required passive spring force is

$$F_{\text{p.s.}} \ge \frac{\tau_m}{r_{\text{crown}}}\frac{(\sin\theta_{\text{crown}} - \mu\cos\theta_{\text{crown}})}{(\cos\theta_{\text{crown}} + \mu\sin\theta_{\text{crown}})} \quad (12)$$

Substituting the parameter values into Eq. (12), the calculated minimum required passive spring force was 0.204 N. The passive spring was selected as

$$F_{\text{p.s.}} = k_{\text{p.s.}}(l_i - l_0) = 0.846\ \text{N} \quad (13)$$

to generate a higher force than the calculated minimum.

The second model (Fig. 7d) was used to calculate the required force of the SMA actuator for triggering. To trigger jumping, the SMA actuator should pull the motor mount and disengage the crown gears. We analyzed this static model when the two gears were about to disengage. The contraction force of the SMA actuator should overcome the friction force between the engaged crown gears and the force applied by the passive spring. Therefore, we calculated the minimum

Table 2 List of parameters for jumping model

Parameters	Description	Value
	Jumping linkage	
l	Length of the jumping linkage	22.7 mm
r	Radius of the bottom round plate of jumping linkage	5 mm
d_1	Distance from center of bottom round plate to center of two bottom joints	5.65 mm
d_2	Distance between two bottom joints	6 mm
d_v	Vertical distance between the center of top two joints to link 5	2.7 mm
d_h	Horizontal distance between the center of top two joints to link 5	14.4 mm
s_1	Distance between from the side joint to the nearest spring anchoring point	4.6 mm
s_2	Distance between from the side joint to the farthest spring anchoring point	8.3 mm
s_0	Initial length of the linear spring	28.3 mm
m_i	Mass of the link i (i = 1, 2, 3, 4)	1.63 g
m_5	Mass of t he link 5	89.18 g
I_i	Moment of the inertia of the link i (i = 1, 2, 3, 4)	69.4 g mm^2
I_5	Moment of inertia of the link 5	78776 g mm^2
ϕ	Angle between the ground and the jumping linkage	75°
k_l	Spring constant of the linear spring	0.1054 N/mm
k_t	Spring constant of the torsional spring	0.635 N mm/deg
	Actuator package	
r_{pulley}	Radius of the spool on which the wire is wound	3 mm
r_{crown}	Radius at midpoint of crown gear tooth	4.9 mm
θ_{crown}	Base angle of the isosceles trapezoid assumed as crown gear teeth	20.22°
μ	Static friction coefficient between two crown gears	0.293
	Selected passive spring	
$k_{\text{p.s.}}$	Spring constant of the selected passive spring	0.1 N/mm
l_0	Initial length of the selected passive spring	10 mm
l_i	Length of the passive spring when two crown gears fully engage	17.42 mm
Δl	Minimum length required for two crown gears to disengage	1.04 mm

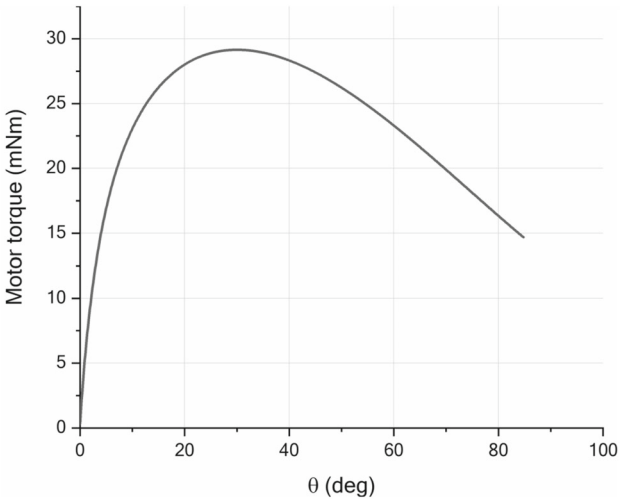

Fig. 6 Required motor torque for energy loading

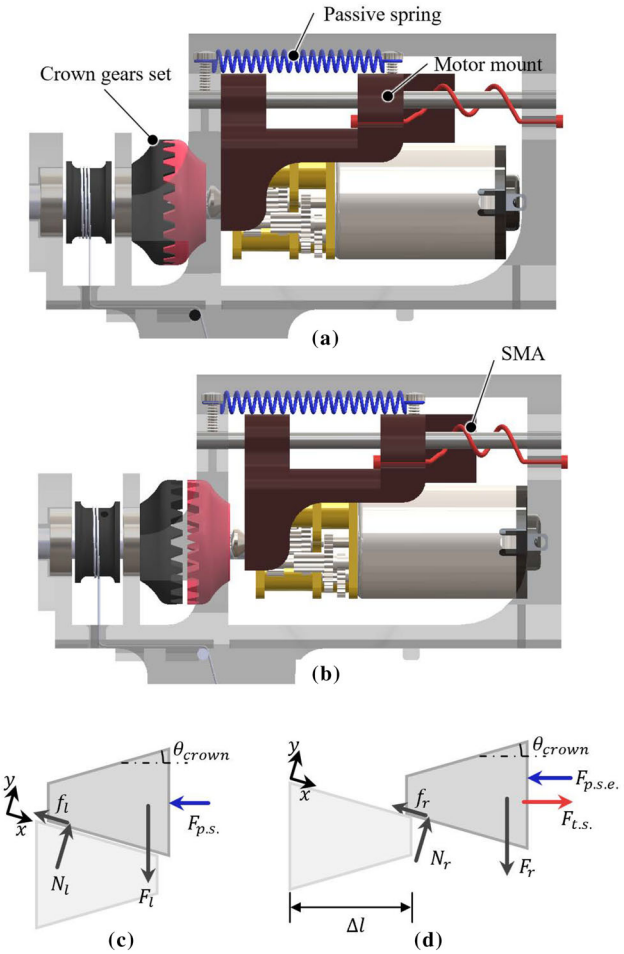

Fig. 7 **a** The passive spring (blue) maintains the engagement between two crown gears. **b** The contraction of the SMA (red) pulls the motor mound rightward and disengages the crown gears. The passive spring Model for selecting **c** passive spring and **d** SMA actuator. The teeth of the crown gears are assumed as trapezoid The applied forces for **a**, **b** are indicated in **c** and (**d**), respectively

SMA force which makes the x-direction component of the net force applied to the motor-connected crown gear become larger than zero (Fig. 7d). The equations describing this procedure are as follows:

$$\Sigma F_x = F_{\mathrm{r}} \sin\theta_{\mathrm{crown}} - F_{\mathrm{p.s.e.}} \cos\theta_{\mathrm{crown}} - f_{\mathrm{r}} + F_{t.s.} \cos\theta_{\mathrm{crown}} \geq 0 \tag{14}$$

$$\Sigma F_y = N_{\mathrm{r}} - F_{\mathrm{r}} \cos\theta_{\mathrm{crown}} - F_{\mathrm{p.s.e.}} \sin\theta_{\mathrm{crown}} + F_{t.s.} \sin\theta_{\mathrm{crown}} = 0 \tag{15}$$

$$F_{\mathrm{r}} = \frac{\tau_f}{r_{\mathrm{crown}}} \tag{16}$$

$$f_{\mathrm{r}} = \mu N_{\mathrm{r}} \tag{17}$$

$$F_{\mathrm{p.s.e.}} = k_{\mathrm{p.s.}}(l_i + \Delta l - l_0) \tag{18}$$

The required SMA contracting force is

$$F_{t.s.} \geq F_{\mathrm{p.s.e.}} - \frac{\tau_{\mathrm{f}}}{r_{\mathrm{crown}}} \frac{(\sin\theta_{\mathrm{crown}} - \mu\cos\theta_{\mathrm{crown}})}{(\cos\theta_{\mathrm{crown}} + \mu\sin\theta_{\mathrm{crown}})} \tag{19}$$

$F_{\mathrm{p.s.e.}}$ is the passive spring force, $F_{t.s.}$ is the SMA contracting force, F_{r} is the spring restoring force acting on the crown gear, N_{r} is the normal reaction force, f_{r} is the friction force between the two crown gears, and τ_{f} is the last value of Fig. (6), 0.0147 Nm. Substituting the parameter values into Eq. (19), the calculated minimum required SMA contracting force was 0.842 N. Also, to disengage the crown gears, the SMA actuator should contract more than 1.04 mm. From these force and displacement requirements, we designed spring-type SMA actuators with a spring diameter of 2 mm using a wire diameter of 0.38 mm by referring [34].

2.2.3 Jumping dynamics

The jumping dynamics was analyzed to estimate the jumping height and distance of the designed mechanism using Lagrangian mechanics. Based on Fig. 5, position P_i and rotation angle R_i of each link are expressed with the generalized coordinate θ.

$$P_1 = \begin{bmatrix} d_1\cos\phi + (\frac{d_2}{2})\sin\phi + (\frac{l}{2})\cos(\phi-\theta) \\ r + d_1\sin\phi - (\frac{d_2}{2})\cos\phi + (\frac{l}{2})\sin(\phi-\theta) \end{bmatrix} \tag{20}$$

$$P_2 = \begin{bmatrix} d_1\cos\phi - (\frac{d_2}{2})\sin\phi + (\frac{l}{2})\cos(\phi+\theta) \\ r + d_1\sin\phi + (\frac{d_2}{2})\cos\phi + (\frac{l}{2})\sin(\phi+\theta) \end{bmatrix} \tag{21}$$

$$P_3 = \begin{bmatrix} d_1\cos\phi + (\frac{d_2}{2})\sin\phi + \\ l\cos(\phi-\theta) + \frac{l}{2}\cos(\phi+\theta) \\ r + d_1\sin\phi - (\frac{d_2}{2})\cos\phi + \\ l\sin(\phi-\theta) + \frac{l}{2}\sin(\phi+\theta) \end{bmatrix} \tag{22}$$

$$P_4 = \begin{bmatrix} d_1\cos\phi - (\frac{d_2}{2})\sin\phi + \\ l\cos(\phi+\theta) + \frac{l}{2}\cos(\phi-\theta) \\ r + d_1\sin\phi + (\frac{d_2}{2})\cos\phi + \\ l\sin(\phi+\theta) + \frac{l}{2}\sin(\phi-\theta) \end{bmatrix} \tag{23}$$

$$P_5 = \begin{bmatrix} d_1\cos\phi + 2l\cos\theta\cos\phi + d_v\cos\phi + d_h\sin\phi \\ r + d_1\sin\phi + 2l\cos\theta\sin\phi + d_v\sin\phi - d_h\cos\phi \end{bmatrix} \tag{24}$$

$$\begin{bmatrix} R_1 \\ R_2 \\ R_3 \\ R_4 \\ R_5 \end{bmatrix} = \begin{bmatrix} \phi-\theta \\ \phi+\theta \\ \phi+\theta \\ \phi-\theta \\ \phi \end{bmatrix} \tag{25}$$

The Lagrangian equation is

$$L = T - V \tag{26}$$

$$\frac{\partial L}{\partial\theta} - \frac{\mathrm{d}}{\mathrm{d}t}\frac{\partial L}{\partial\dot{\theta}} = 0 \tag{27}$$

where the kinetic energy T and the potential energy V are

$$T = \frac{1}{2}\sum_{i=1}^{5} m_i \|\dot{P}_i\|^2 + \frac{1}{2}\sum_{i=1}^{5} I_i \dot{R}_i{}^2 \tag{28}$$

$$V = 4\times\frac{1}{2}k_t\theta^2 + \frac{1}{2}k_l(s(\theta)-s_0)^2 + \sum_{i=1}^{5} m_i g P_{i,y} \tag{29}$$

For $s(\theta)$ refer to Eq. (1). We set the value of the θ when the robot started to push off as an initial condition and zero as the initial time rate of the θ.

$$\begin{bmatrix} \theta_0 \\ \dot{\theta}_0 \end{bmatrix} = \begin{bmatrix} 74.2^\circ \\ 0 \end{bmatrix} \tag{30}$$

By solving (MATLAB, ODE45 solver) this initial value problem, the θ with respect to the time t, $\theta(t)$, is calculated. Substituting the result to Eqs. (20)–(24) and with the time derivatives, the position, velocity, and acceleration of each link can be obtained. The take-off occurs when the vertical reaction force $V(t)$ becomes zero, so the take-off time t_f can be calculated.

$$\sum_{i=1}^{5} m_i \ddot{P}_{i,y}(t) = V(t) - \sum_{i=1}^{5} m_i g \tag{31}$$

$$V(t_f) = 0 \tag{32}$$

where $\ddot{P}_{i,y}$ is the acceleration of link i in the y-direction, and g is the gravitational acceleration. The take-off velocity v_f and take-off angle ψ_f can be obtained by calculating the velocity of CoM at the take-off time.

$$v_{f,x} = \sum_{i=1}^{5} m_i \dot{P}_{i,x}(t_f) / \sum_{i=1}^{5} m_i \tag{33}$$

$$v_{f,y} = \sum_{i=1}^{5} m_i \dot{P}_{i,y}(t_f) / \sum_{i=1}^{5} m_i \tag{34}$$

$$v_f = \sqrt{v_{f,x}^2 + v_{f,y}^2} \tag{35}$$

$$\psi_f = \tan^{-1}\left(\frac{v_{f,y}}{v_{f,x}}\right) \tag{36}$$

The calculated take-off velocity was 2.247 m/s with a take-off angle of 75°. Assuming the ideal ballistic jumping, the jumping height H and distance D can be calculated as follows:

$$H = \frac{{v_f}^2 \sin^2 \psi_f}{2g} \tag{37}$$

$$D = \frac{2{v_f}^2 \sin \psi_f \cos \psi_f}{g} \tag{38}$$

The robot can jump with a height of 24 cm and a distance of 25.8 cm.

2.3 Self-righting mechanism

The robot overturns after jumping because the extended jumping linkage protrudes ventrally. Therefore, a self-righting mechanism is necessary for the post-jumping operation, and we employed a wing opening mechanism for self-righting (Fig. 8). When the robot is flipped, it opens its wings, and the flipped body is lifted and recovers its upright posture. Subsequently, the robot folds its wings to avoid collisions.

The self-righting mechanism is composed of two wings, the Sarrus linkage, and the leadscrew actuator. For a compact and light design, the Sarrus linkage is designed using the SCM method. The wings are separately attached to the rotating links of the linkage, the leadscrew nut is attached to one of the translating plates of the linkage, and the other plate is grounded with the robot body. The linear motion of the nut controls the wing opening and folding (Fig. 8b–d).

To successfully upright the flipped robot, the wings should be opened enough to let the center of mass (CoM) pass over the critical point between the robot and the ground that lies in the plane $x_0 z_0$ in Fig. 9a, and the motor torque should be sufficient to lift the weight of the robot. The opening angle of the wing is determined by the ratio of the length of the two sides of the Sarrus linkage and the actuation displacement. Therefore, we calculated the kinematics of the Sarrus linkage and the position of the CoM to validate the proper selection of the design parameters. We built a simplified model of the self-righting process as shown in Fig. 9. The robot is initially flipped over as Fig. 9a. As the linear actuation of the Sarrus

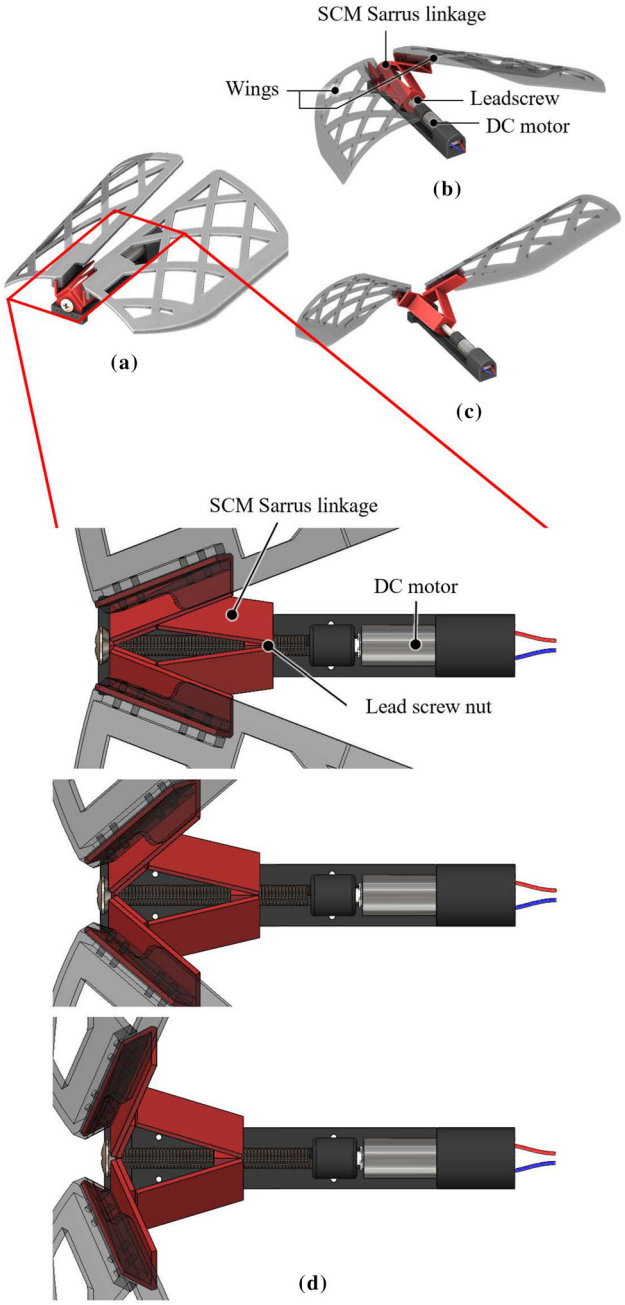

Fig. 8 Detailed composition of the self-righting mechanism. **a** Frontal view of the closed wings. **b** Hind view of the closed wings. **c** Hind view of the opened wings. **d** Sequences of motion of the Sarrus linkage while wing opening. Actuation of the motor moves the lead screw nut leftward and it opens the wings

linkage occurs like Fig. 9b, the linkage is lifted from the ground, so it makes the CoM to rotate about x_0-axis. The amount of rotation is α_1. We assumed the robot and its wings were symmetric along the sagittal plane of the robot. The kinematics of the Sarrus linkage with respect to the linear displacement of the actuator was calculated with the Denavit-Hartenberg (DH) parameters listed in Table 3. l_1 is the length

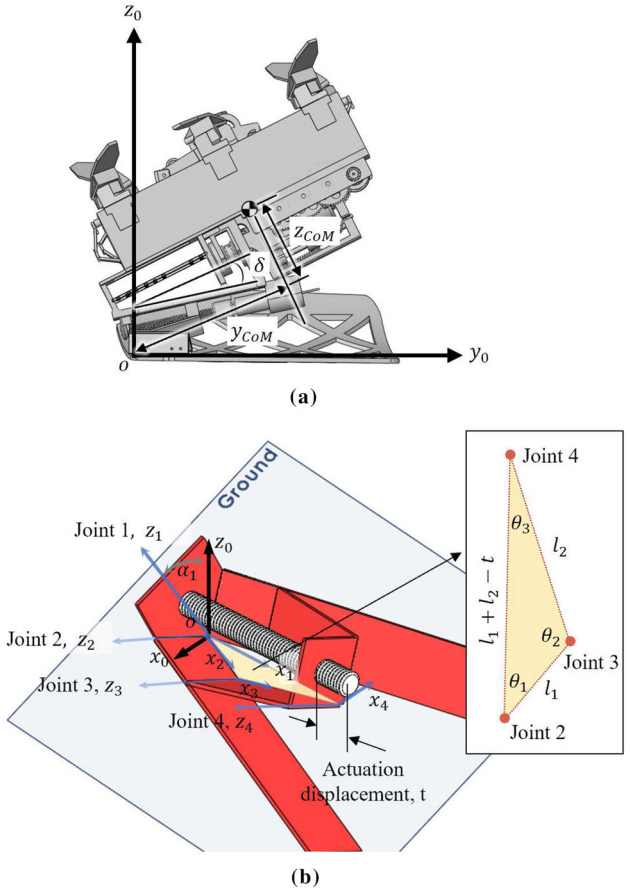

Fig. 9 Model for self-righting mechanism. **a** The robot is flipped over and the wings are in contact with the ground. **b** Simplified model for calculating the kinematics of Sarrus linkage. The joints and axes for DH parameters are highlighted in blue

Table 3 DH parameters for the self-righting linkage

	α_{i-1}	a_{i-1}	d_i	θ_i
1	α_1	0	0	$\pi/2$
2	$\pi/4$	0	0	$-\theta_1$
3	0	l_1	0	$\pi - \theta_2$
4	0	l_2	0	$\pi/2 - \theta_3$

of the shorter side of the Sarrus linkage, l_2 is the length of the longer side, t is the actuation displacement, and θ_1,θ_2,θ_3 are the corner angles of the triangle formed by the three joints in the Sarrus linkage, as shown in Fig. 9b.

One of the links on the side of the Sarrus linkage, containing joint 2 and joint 3, is attached to the wing. In the flipped posture, the inner edge of this link always remains in contact with the ground. Therefore, the origin of joint 3 represented in coordinate O should be zero.

$$T_{0,3} = T_{0,1}T_{1,2}T_{2,3} \tag{39}$$

$$T_{0,3}(3,4) = 0 \tag{40}$$

where the transform matrix for the adjacent coordinate frame $T_{i-1,i}$ is defined as Eq. (41).

$$T_{i-1,i} = \begin{bmatrix} \cos\theta_i & -\sin\theta_i & 0 & a_{i-1} \\ \sin\theta_i \cos\alpha_{i-1} & \cos\theta_i \cos\alpha_{i-1} & -\sin\alpha_{i-1} & -d_i \sin\alpha_{i-1} \\ \sin\theta_i \sin\alpha_{i-1} & \cos\theta_i \sin\alpha_{i-1} & \cos\alpha_{i-1} & d_i \cos\alpha_{i-1} \\ 0 & 0 & 0 & 1 \end{bmatrix} \tag{41}$$

Simplifying Eq. (40) results in Eq. (42).

$$\tan\alpha_1 = \frac{\sqrt{2}}{2}\tan\theta_1 \tag{42}$$

where

$$\theta_1 = \cos^{-1}\left(\frac{(l_1 + l_2 - t)^2 + {l_2}^2 - {l_1}^2}{2l_2(l_1 + l_2 - t)}\right) \tag{43}$$

We can calculate the rotating angle of the Sarrus linkage relative to the ground α_1 with respect to the actuation displacement t by Eqs. (42)–(43).

The Sarrus linkage was attached to the robot frame at the angle of δ, and we assumed the symmetry of the robot with respect to the sagittal plane (Fig. 9a). Therefore, the location of the CoM while actuating the Sarrus linkage in coordinate O can be calculated by rotating the initial position of the CoM about the x_0 axis by an angle of $\delta + \alpha$.

$$P_{0,\mathrm{CoM}} = \begin{bmatrix} 1 & 0 & 0 \\ 0 & \cos(\delta + \alpha_1) & -\sin(\delta + \alpha_1) \\ 0 & \sin(\delta + \alpha_1) & \cos(\delta + \alpha_1) \end{bmatrix} \begin{bmatrix} 0 \\ y_{\mathrm{CoM}} \\ z_{\mathrm{CoM}} \end{bmatrix} \tag{44}$$

Then, we need to verify that the available actuation displacement, which is 16 mm for the current design, can make the CoM pass across the critical point on the z_0 axis. We calculated the required actuation displacement t_{offset} when the y-coordinate of the CoM became y_{offset} with a margin of 2 cm from the critical point for safe design. Figure 10a illustrates the y-coordinate of the CoM with respect to the actuation displacement by substituting the parameter values (l_1 = 8 mm, l_2 = 16 mm, δ = 14.5°, y_{CoM} = 45 mm, z_{CoM} = 30 mm, y_{offset} = −20 mm). The required actuation displacement t_{offset} when the CoM reaches the y_{offset}, which is less than the maximum actuation displacement. This implies that the current Sarrus linkage can flip over the robot body. Figure 10b shows the trajectory of the CoM for for $t < t_{\mathrm{offset}}$.

To calculate the required motor torque to lift the flipped robot, we calculated the gravitational potential energy V_p and its partial derivative with respect to the actuation displacement t. With the quasi-static assumption, this partial

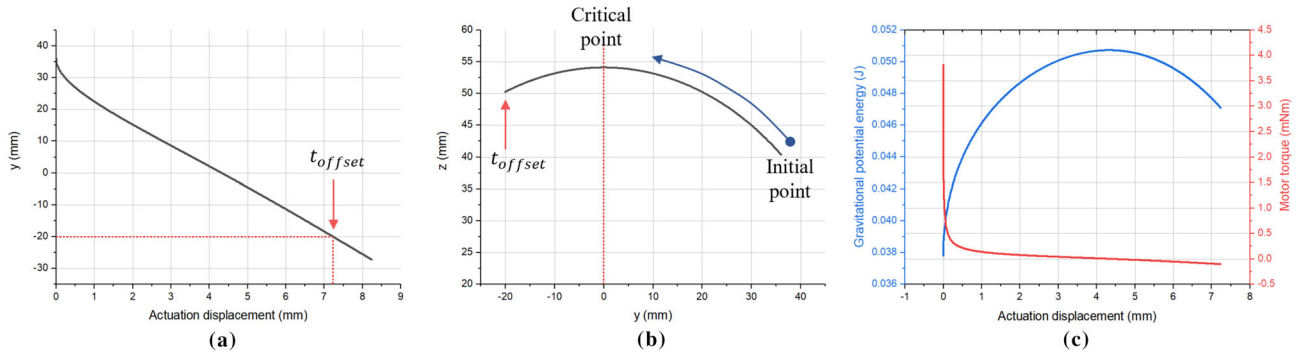

Fig. 10 **a** The y-coordinate of the CoM with respect to the actuation displacement. **b** The position of CoM while the actuation. The y-coordinate of the CoM becomes negative, which means that the CoM can pass over the pivot point to the ground. **c** The gravitational potential energy and required motor torque with respect to the actuation displacement

derivative can be regarded as the required force for linear actuation. Then, the required motor torque can be converted with this force and the parameters of the lead screw where L is the screw lead, η is the efficiency, and m is the total mass of the robot ($L = 0.5$ mm, $\eta = 0.2$, $m = 95.7$ g).

$$\tau_{\text{righting}} = \frac{L}{2\pi\eta}\left(-\frac{\partial V_p}{\partial t}\right) \tag{45}$$

$$V_p = mgP_{0,\text{CoM}} \tag{46}$$

As shown in Fig. 10c, the maximum required torque is 3.8 mNm, so we chose a DC motor with a higher torque output.

2.4 Integration

The crawling, jumping, and self-righting mechanisms are integrated into a single body. To arrange as compactly as possible without interfering with the range of motion of each mechanism, the jumping mechanism is placed on the medioventral side of the crawling mechanism, and the self-righting mechanism is placed above the crawling and jumping mechanisms. The size of the robot is (length) 9.8 cm × (width) 9 cm × (height) 8.8 cm when the wings and the jumping linkage are folded. The mass of the entire robot including the controller and batteries is 95.7 g, and the mass budget of each component is described in Table 4.

The SCM designed mechanisms were fabricated with a PET of 400 μm thickness as facets and ripstop fabric of 150 μm thickness as flexures. The rest of the parts were 3D-printed. The crawling motors are MK07-10 from Didel, and a custom-made 64:1 gearbox (one pinion and three stages of 4:1 compound gear, G312 and G348, Didel) was applied. The jumping motor was a 298:1 micrometal gearmotor from Pololu. The SMA actuator uses a diameter of 0.38 mm, 70 °C Flexinol Actuator Wire from DYNALLOY Inc, and it is annealed at 350 °C for 1 h. The self-righting motor was an LCP06-A03V-0700 from D&J WITH Co., Ltd. The custom-made leadscrew is composed of an M3 plastic bolt and nut. CurieNano (DFRobot) was used as a controller, and three dual H-bridge DC motor drivers (HR8833, DFRobot) were used to control the motors and SMA actuators. Two 3.7 V, 100 mAh LiPo batteries were used. For remote control, we used BLE communication with the Blynk application.

Table 4 Mass budget of components

Component	Mass (g)	Portion(%)
Crawling mechanism	31.6	33
Jumping mechanism	28.85	30.1
Self-righting mechanism	11.91	12.4
Controller	16.26	17
Batteries	7.08	7.4
Total	95.7	100

3 Result

Experiments were conducted to examine the performance of each mechanism. Crawling speed, jumping height and distance, and self-righting duration were evaluated. In addition, we measured the energy consumption of each function. All experimental results were calculated by averaging five trials. Also, demonstrations were performed to show the advantages and usability of the proposed small-scale jumping–crawling robot.

3.1 Crawling

A crawling performance experiment was conducted to measure the crawling speed. The experiment was conducted on a flat foam board track. Crawling speed was calculated by measuring the time required for the robot to crawl at 180 cm. From

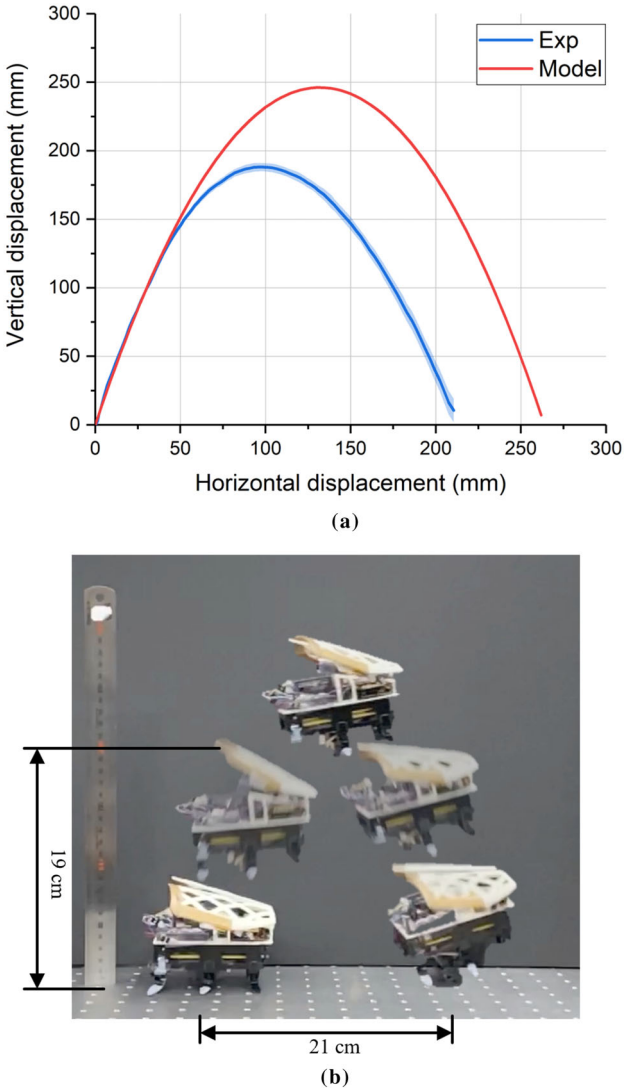

Fig. 11 Jumping performance of the robot. **a** Comparison of experimental and dynamic model result. The robot jumps 19 cm in height and 21 cm in distance. **b** Snapshot of one case of jumping motion

these five trials, we obtained the average crawling speed. The crawling speed of this robot was 3.94 cm/s, which is 0.4 BL/s.

3.2 Jumping

A jumping performance experiment was conducted to measure the jumping height and distance of the robot. The robot was placed on flat ground, and the jumping motion was recorded. The jumping height and distance were measured, as illustrated in Fig. 11. The robot can jump 19 cm in height, which is 2.2 times the body height, and 21 cm in distance, which is 2.1 times the body length.

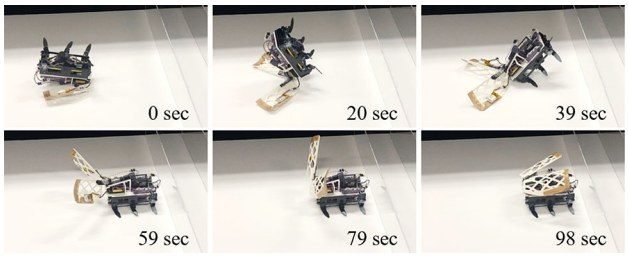

Fig. 12 Self-righting of the robot. The snapshot of self-righting process of one case is illustrated with timestamp. Self-righting takes 52.5 s and wing folding takes 50.1 s

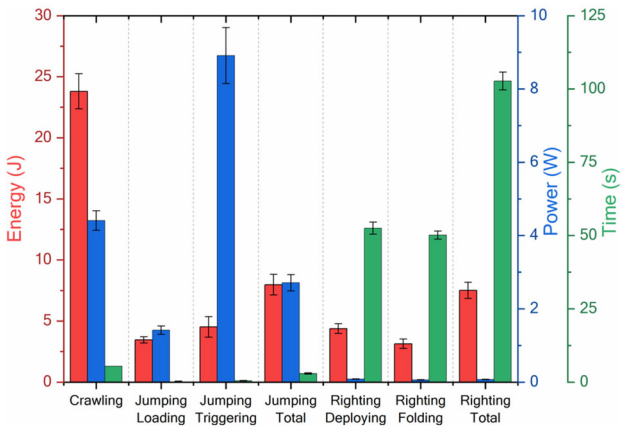

Fig. 13 Comparison of power and time consumption and required energy for performing each function

3.3 Self-righting

The self-righting performance was conducted to measure the time taken by the robot to upright its posture. We placed the robot in a flipped-over posture on the foam board and recorded self-righting. It took 52.5 s to self-right with wing opening, and 50.1 s to fold the wing again, for a total of 102.6 s (Fig. 12).

3.4 Energy consumption

The energy consumption for crawling, jumping, and self-righting was measured to estimate the operating time or repeatable count for each function. We applied 3.7 V using a power supply and measured the current for one cycle of each motion, and then calculated the average current. Crawling needs 1.19 A for maximum speed. To compare the energy consumption with the jumping, we calculated the energy while it crawls the same distance for jumping, which takes 5.4 s for 21 cm. For jumping, the energy loading requires 0.384 A during 2.44 s and the triggering with the SMA actuator requires 2.41 A during 0.5 s, so one jump consumes 7.974 J with 2.95 s. We also measured the temperature of the SMA actuator with the thermal camera when energy release

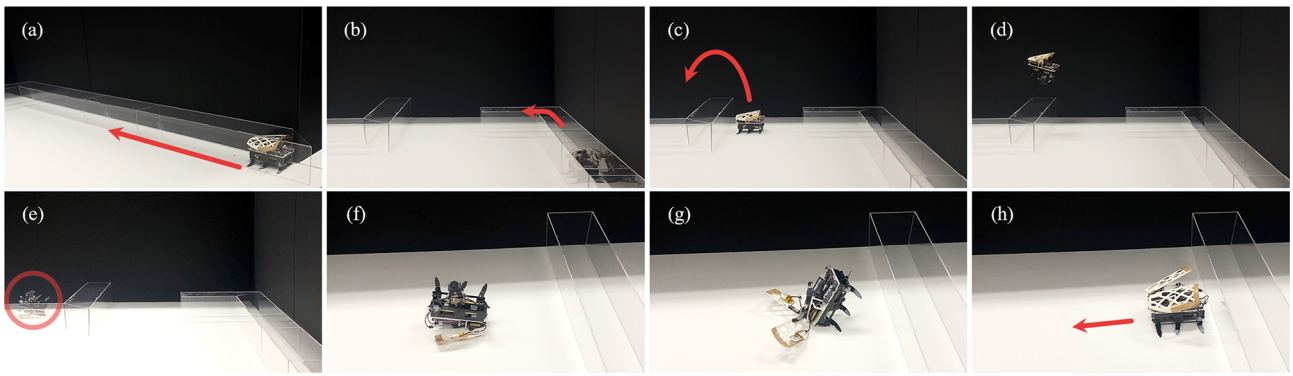

Fig. 14 Demonstration on the mockup track. **a**–**b** The robot crawls through the pipeline. **c**–**e** The robot jumps over the pipe. **f** The robot folds the extruded jumping linkage. **g** The robot self-rights its posture. **h** The robot crawls again

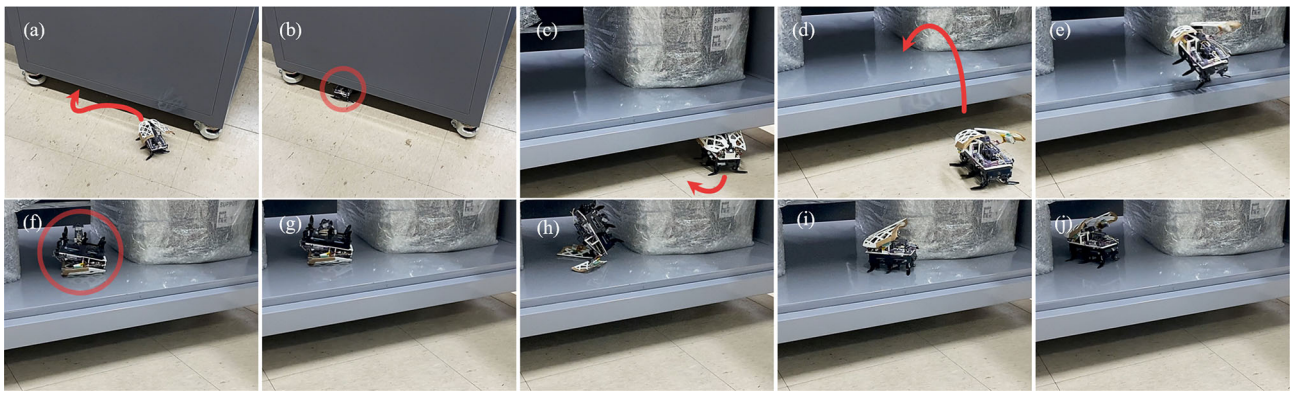

Fig. 15 Demonstration in the laboratory. **a**–**c** The robot crawls through under the shelf. **d**–**f** The robot jumps up to the shelf. **g** The robot folds the extruded jumping linkage. **h**, **i** The robot self-rights its posture. **j** The robot crawls again

occurred, and the temperature changed from 31.3 to 48.06 °C. Self-righting takes 0.022 A with 52.5 s for upright its posture by opening the wing and 0.017 A with 50.1 s for wing folding, so it requires 7.72 J during 102.6 s. Figure 13 illustrates the results of required power and time, and resultant energy consumption for each function.

Assuming using the battery capacity of 200 mAh only for each function, we calculated the operating time for crawling and repeatable count for jumping and self-righting. This robot can crawl for approximately 10 min with a distance of 2364 cm, jump 334 times, and self-right 354 times. However, the robot should perform self-righting after jumping to reoperate other functions because the protrusion of the jumping linkage causes a flipped posture. Therefore, we also calculated the repeatable count for performing both jumping and self-righting in a row, which was 172 times.

3.5 Demonstration

Multi-modal demonstrations were conducted to show the potential use of the proposed small-scale jumping–crawling robot. The robot can crawl in the open field or inside small gaps, and when the robot encounters an obstacle, it can jump over the obstacles about double its height. In addition, when the robot overturns after jumping, it folds the jumping linkage and opens the wings to self-right. Then, it can crawl again. We demonstrated two environments: one is a mockup track, the other is an actual laboratory. In Fig. 14, we constructed the mockup track with acrylic pipes with the width of 95 cm and height of 88 cm. The robot crawls through the pipeline and jumps over the other pipe to travel beyond the pipe. As shown in Fig. 15, the demonstration was performed in the laboratory. There is a shelf with an 8 cm height gap from the floor. To go inside the shelf, the robot should overcome the hurdle of 13.5 cm. The robot crawls under the shelf and jumps up to go inside the shelf.

4 Conclusion

In this paper, we proposed a sub-10 cm, sub-100 g jumping–crawling robot. To meet the weight and size limits, SCM-

based linkage structures were implemented into the crawling and self-righting mechanisms. Also, a compact actuator package was designed for energy loading and triggering of the jumping mechanism. Based on the analytical model, the DC motor and SMA actuators in the actuator package were selected carefully. In addition to all locomotive mechanisms, electronic components, controller and batteries, were integrated into the robot for untethered operation. As a result, the robot can crawl 3.94 cm/s (0.4 BL/s), jump 19 cm (2.2 BH) height and 21 cm (2.1 BL) far. To show the applicability of the proposed small-scale robot, two demonstrations were performed. The robot can crawl through the confined space and jump over obstacles. Also, the robot can upright its posture from the overturn to continue operating after jumping. We believe that the robot with the proposed scale can be easily carried and operated by individuals in places where people are, and it can be adopted for the swarm robotic applications.

5 Supplementary information

This paper includes a supplementary video.

Supplementary Information The online version contains supplementary material available at https://doi.org/10.1007/s11370-023-00497-z.

Acknowledgements This research is performed based on the cooperation with the Defense Acquisition Program Administration and Defense Rapid Acquisition Technology Research Institute's Critical Technology R&D program (No. UC190002D).

References

1. Birkmeyer P, Peterson K, Fearing RS (2009) DASH: a dynamic 16g hexapedal robot. In: Proceedings of the IEEE/RSJ international conference on intelligent robots and systems. St. Louis, MO, USA, pp 2689–2689. https://doi.org/10.1109/IROS.2009.5354561
2. Kim S, Clark E, Cutkosky MR (2006) iSprawl: design and tuning for high-speed autonomous open-loop running. Int J Robot Res 25(9):903–912. https://doi.org/10.1177/0278364906069150
3. Morrey B, Lambrecht AD, Horchler RE et al (2003) Highly mobile and robust small quadruped robots. In: Proceedings of the IEEE/RSJ international conference intelligent robots systems. Las Vegas, NV, USA, pp 2689–2689. https://doi.org/10.1109/IROS.2003.1250609
4. Saranli U, Buehler M, Koditschek DE (2001) RHex: a simple and highly mobile hexapod robot. Int J Robot Res 20(7):616–631. https://doi.org/10.1177/0278364012206757
5. Zarrouk D, Pullin A, Kohut N et al (2013) STAR, a sprawl tuned autonomous robot. In: Proceedings of the IEEE international conference on robotics automation. Karlsruhe, Germany, pp 20–25. https://doi.org/10.1109/ICRA.2013.6630551
6. Mi J, Wang Y, Li C (2022) Omni-roach: A legged robot capable of traversing multiple types of large obstacles and self-righting. In: Proceedings of the IEEE international conference on robotics automation. Philadelphia, PA, USA, pp 20–25. https://doi.org/10.1109/ICRA46639.2022.9811372
7. Kovac M, Fuchs M, Guignard A et al (2008) A miniature 7g jumping robot. In: Proceedings of the IEEE International Conference on Robotics Automation. Pasadena, CA, USA, pp 373–378. https://doi.org/10.1109/ROBOT.2008.4543236
8. Zhao J, Xu J, Gao B et al (2013) MSU jumper: a single-motor-actuated miniature steerable jumping robot. IEEE Trans Robot 29(3):602–614. https://doi.org/10.1109/TRO.2013.2249371
9. Haldane DW, Plecnik MM, Yim JK et al (2016) Robotic vertical jumping agility via series-elastic power modulation. Sci Robot 1(1):eaag2048. https://doi.org/10.1126/scirobotics.aag2048
10. Yim S, Baek SM, Jung GP et al (2018) An omnidirectional jumper with expanded movability via steering, self-righting and take-off angle adjustment. In: Proceedings of the IEEE/RSJ international conference on intelligent robots and systems. Madrid, Spain, pp 416–421. https://doi.org/10.1109/IROS.2018.8594372
11. Kim S, Spenko M, Trujillo S et al (2008) Smooth vertical surface climbing with directional adhesion. IEEE Trans Robot 24(1):65–74. https://doi.org/10.1109/TRO.2007.909786
12. Asbeck AT, Cutkosky MR (2012) Designing compliant spine mechanisms for climbing. J Mech Robot 4(3):031007. https://doi.org/10.1115/1.40066591
13. Murphy MP, Sitti M (2007) Waalbot: an agile small-scale wall-climbing robot utilizing dry elastomer adhesives. IEEE/ASME Trans Mechatron 12(3):330–338. https://doi.org/10.1109/TMECH.2007.897277
14. Spenko MJ, Haynes GC, Saunders JA et al (2008) Biologically inspired climbing with a hexapedal robot. J F Robot 25(4–5):223–242. https://doi.org/10.1002/rob.20238
15. Full RF, Tu MS (1991) Mechanics of a rapid running insect: two-, four- and six-legged locomotion. J Exp Biol 156(1):215–231. https://doi.org/10.1242/jeb.156.1.215
16. Sutton GP, Burrows M (2011) Biomechanics of jumping in the flea. J Exp Biol 214(5):836–847. https://doi.org/10.1242/jeb.052399
17. Autumm K, Sitti M, Liang YA et al (2002) Evidence for van der Waals adhesion in gecko setae. Proc Natl Acad Sci 99(19):12252–12256. https://doi.org/10.1073/pnas.192252799
18. Lambrecht BGA, Horchler AD, Quinn RD (2005) A small, insect-inspired robot that runs and jumps. In: Proceedings of the IEEE international conference on robotics and automation. Spain, pp 1240–1245. https://doi.org/10.1109/ROBOT.2005.1570285
19. Jung GP, Casares CS, Lee J et al (2019) JumpRoACH: a trajectory-adjustable integrated jumping–crawling robot. IEEE/ASME Trans Mechatron 24(3):947–958. https://doi.org/10.1109/TMECH.2019.2907743
20. Chae SH, Baek SM, Lee J et al (2022) Agile and energy-efficient jumping–crawling robot through rapid transition of locomotion and enhanced jumping height adjustment. IEEE/ASME Trans Mechatron 27(6):5890–5901. https://doi.org/10.1109/TMECH.2022.3190673
21. Zhakypov Z, Mori K, Hosoda K et al (2019) Designing minimal and scalable insect-inspired multi-locomotion millirobots. Nature 571(7765):381–386. https://doi.org/10.1038/s41586-019-1388-8
22. Hu W, Lum GZ, Mastrangeli M et al (2018) Small-scale soft-bodied robot with multimodal locomotion. Nature 554(7690):81–85. https://doi.org/10.1038/nature25443
23. Zhao J, W Y, Xi N et al (2005) A miniature 25 grams running and jumping robot. In: Proceedings of the IEEE international conference on robotics automation. Hong Kong, China, pp 5115–5120. https://doi.org/10.1109/ICRA.2014.6907609
24. Vidyasagar A, Zufferey JC, Floreano D et al (2015) Performance analysis of jump-gliding locomotion for miniature robotics. Bioinspir Biomim 10(2):025006. https://doi.org/10.1088/1748-3190/10/2/025006
25. Desbiens AL, Pope MT, Christensen DL et al (2014) Design principles for efficient, repeated jumpgliding. Bioinspir Biomim 9(2):025009. https://doi.org/10.1088/1748-3182/9/2/025009

26. Baek SM, Yim S, Chae SH et al (2020) Ladybird beetle-inspired compliant origami. Sci Robot 5(41):6262. https://doi.org/10.1088/1748-3182/9/2/025009
27. Woodward MA, Sitti M (2014) MultiMo-Bat: a biologically inspired integrated jumping-gliding robot. Int J Robot Res 33(12):1511–1529. https://doi.org/10.1177/0278364914541301
28. Pope MT, Kimes CW, Jiang H et al (2017) A multimodal robot for perching and climbing on vertical outdoor surfaces. IEEE Trans Robot 33(1):38–48. https://doi.org/10.1109/TRO.2016.2623346
29. Dickson JD, Clark JE (2013) Design of a multimodal climbing and gliding robotic platform. IEEE/ASME Trans Mechatron 18(2):494–505. https://doi.org/10.1109/TMECH.2012.2223708
30. Alexander RM (2003) Principles of animal locomotion. Princeton University Press, Princeton
31. Lee J, Jung GP, Baek SM et al (2020) CaseCrawler: a lightweight and low-profile crawling phone case robot. IEEE Robot Autom Lett 5(4):5858–5865. https://doi.org/10.1109/LRA.2020.3010205
32. Kaspari M, Weiser MD (1999) The size-grain hypothesis and interspecific scaling in ants. Funct Ecol 13(4):530–538. https://doi.org/10.1046/j.1365-2435.1999.00343.x
33. Wood RJ, Avadhanula S, Sahai R et al (2008) Microrobot design using fiber reinforced composites. J Mech Des 130(5):052304. https://doi.org/10.1115/1.2885509
34. An SM, Ryu J, Cho M et al (2012) Engineering design framework for a shape memory alloy coil spring actuator using a static two-state model. Smart Mater Struct 21(5):055009. https://doi.org/10.1088/0964-1726/21/5/055009